analytical chemistry

pubs.acs.org/ac Article

Ultrasensitive Photoelectrochemical Biosensor Based on Novel Z-Scheme Heterojunctions of Zn-Defective CdS/ZnS for MicroRNA Assay

Xiankang Niu, Yan Zhao, Fang Wang, Jinghua Wu, Fengli Qu,* and Weihong Tan

Cite This: *Anal. Chem.* 2021, 93, 17134−17140 Read Online

ACCESS | Metrics & More | Article Recommendations | Supporting Information

ABSTRACT: The sensitive and accurate detection of microRNA (miRNA) has meaningful values for clinical diagnosis application as an early stage of tumor markers. Herein, a novel photoelectrochemical (PEC) biosensor was developed for the ultrasensitive and highly selective detection of microRNA-122 (miRNA-122) based on a direct Z-scheme heterojunction of Zn vacancy-mediated CdS/ZnS (CSZS−V_{Zn}). Impressively, the prepared Z-scheme heterojunction nanocomposite with defect level properties could make the photogenerated charges stay at the Zn vacancy defect levels and combine photogenerated holes in the valence bands of CdS, thus significantly achieving a better charge carrier separation efficiency and broadening the absorption of visible light and demonstrating 5−8 times enhancement of PEC response compared to single-component materials. Simultaneously, an exonuclease III (Exo-III)-assisted signal amplification strategy and a strand displacement reaction were combined to improve the conversion efficiency of the target and further increase the detection sensitivity. More importantly, the elaborated biosensor showed ultrasensitive and highly specific detection of the target miRNA-122 over a wide linear range from 10 aM to 100 pM with a low detection limit of 3.3 aM and exhibited enormous potential in the fields of bioanalysis and clinical diagnosis.

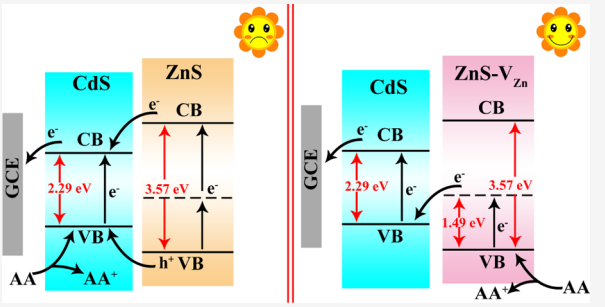

INTRODUCTION

Photoelectrochemical (PEC) bioanalysis has been extensively explored and developed over the past decade with a higher sensitivity, lower background noise, and faster response compared with traditional electrochemical methods, along with simpler and easier operation in terms of apparatus than the optical methods.[1−4] Notably, photoactive materials play important roles in the proposed PEC biosensor as their superior photocurrent intensity and detection sensitivity properties directly determine the efficiency of PEC biosensors.[5] Up to now, numerous inorganic semiconductor materials such as metal oxides, carbon materials, and sulfides have been widely used in PEC assay with excellent photoelectric performance.[6,7] Nevertheless, the conversion efficiency of these semiconductor nanomaterials is primarily limited due to a high electron−hole pair recombination rate and poor light absorption capacity in actual analysis.[8,9] In recent years, the homojunction strategies using single semiconductor components and heterojunctions by utilizing multiple semiconductor components have been proven to promote the separation of electron−hole pairs and inhibit the recombination of electron−hole pairs.[10,11] Compared to homojunctions, heterojunctions could not only overcome the deficiencies of weak light absorption capacity but also exhibit remarkable physicochemical properties.[12] Therefore, it is essential to develop unique heterojunction-based nanomaterials for PEC bioanalysis.

Recently, some heterojunction-type nanomaterials have been reported to improve the energy band structure, such as type-I, type-II, Schottky junction, S-step heterojunction, and Z-scheme.[13−17] Among them, the Z-scheme heterojunction provides additional advantages in maintaining the redox potential and improving the charge carrier separation efficiency.[18] Additionally, the light absorption of most heterojunction inorganic semiconductors is limited by the UV region (<387 nm), leading to a low light utilization rate and thus severely restricting its development and application in PEC bioanalysis. The key factor of these challenges is energy bandwidth.[19,20] Therefore, it is essential to increase the charge separation efficiency by improving the energy band structure. Fortunately, defect engineering in semiconductors can improve the interfacial contacts within them by transforming type-I/type-II heterojunctions into Z-scheme heterojunctions, which can effectively restrain the recombination of electron−hole

Received: November 6, 2021
Accepted: December 3, 2021
Published: December 16, 2021

https://doi.org/10.1021/acs.analchem.1c04820
Anal. Chem. 2021, 93, 17134−17140

Scheme 1. Schematic Illustration of (A) Highly Efficient Exo III-Assisted Cycling Amplification, (B) Assembly of the PEC Biosensor, and (C) Photocurrent Response with or without Target miRNA-122

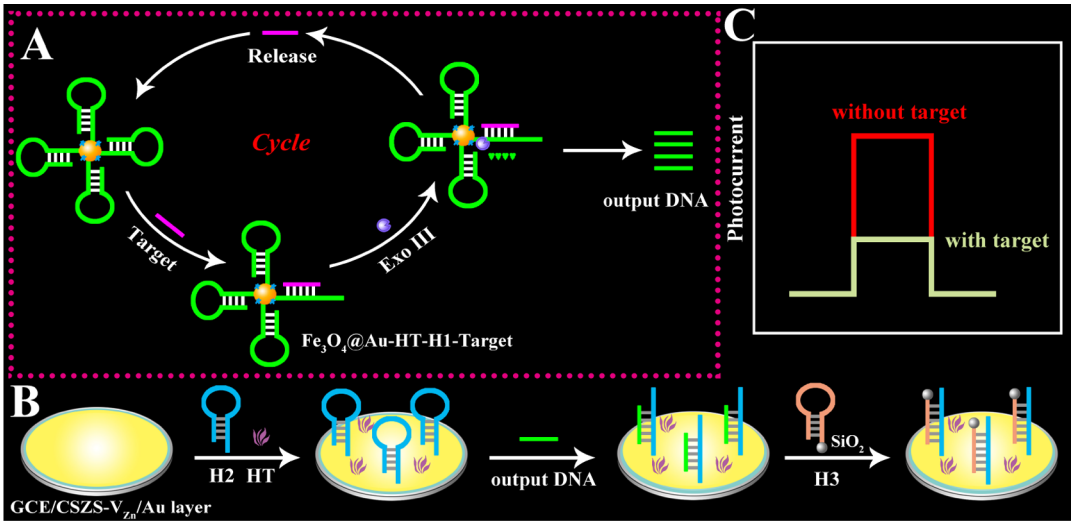

pairs. According to reports, the heterostructure of charge transfer in the oxygen vacancies of CdS/$CdWO_4$ was switched from type-II to Z-scheme.[21] Furthermore, defect engineering could optimize the energy band structure of semiconductors by introducing vacancy defects into the band gap width, thus extending the absorption range of the absorbed wave and enhancing the utilization of light energy.[18] Lately, Wang's group found that titanium-deficient TiO_2 exhibited a significantly higher photocatalytic activity compared to traditional TiO_2.[22] Zou's group demonstrated that the introduction of zinc vacancies in the ZnS structure resulted in a remarkably higher photoactivity compared with that of traditional ZnS.[23] Inspired by above development, a Z-scheme heterojunction based on Zn vacancy CdS/ZnS−V_{Zn} (CSZS−V_{Zn}) was constructed with excellent PEC performance and great potential for application in biosensors.

It is confirmed that the abnormal expression levels of microRNAs can be used as a crucial diagnostic indicator of cancer.[24,25] Herein, we proposed a novel PEC biosensor based on the Zn vacancy defect-mediated direct Z-scheme CSZS−V_{Zn} heterostructure for ultrasensitive detection of microRNA-122 (miRNA-122) using a highly efficient enzyme-assisted cycle amplification strategy. As shown in Scheme 1, CSZS−V_{Zn} was coated on a polished glass carbon electrode (GCE) to furnish an initial photocurrent response which demonstrated five−eightfold enhancement compared to single-component materials (Figure S2). Then, gold nanoparticles (Au NPs) were employed for immobilizing hairpin DNA2 (H2) by Au−S bonds followed by blocking unbound sites with hexanethiol (HT). Moreover, a tiny amount of target miRNA-122 was transformed into plenty of output DNA, which could hybridize with H2 to produce abundant DNA duplexes by using the exonuclease III (Exo III)-assisted signal amplification strategy. Finally, hairpin DNA3 (H3) with SiO_2 NPs labeled at the 5′ end would lead to the formation of H2/H3 duplexes *via* the strand displacement reaction (SDR), making SiO_2 NPs close to the electrode surface and resulting in highly efficient quenching of the PEC signal response, owing to the large steric hindrance effect, consequently achieving a sensitive assay of miRNA-122. This exclusive design provides a new insight for the accurate detection of biomolecules, early cancer diagnosis, and clinical cancer monitoring.

EXPERIMENTAL SECTION

Synthesis of CSZS−V_{Zn}, SiO_2−COOH NPs, and Fe_3O_4@Au. Precursors of CdS and Zn-defected ZnS (ZnS−V_{Zn}) were prepared following the protocols reported previously.[23] Briefly, the CSZS−V_{Zn} heterostructure was synthesized using a simple hydrothermal method. First, 3 mmol $Na_2S{\cdot}9H_2O$, 3 mmol $Cd(Ac)_2{\cdot}2H_2O$, and 2 mmol as-prepared ZnS−V_{Zn} were dissolved in 40 mL of ultrapure water with continuous stirring for 15 min. Subsequently, the aforementioned solution was transferred to a Teflon-lined stainless-steel autoclave and then heated to 160 °C for 14 h. Finally, the obtained precipitate was purified by centrifugation and washing with ethanol and ultrapure water and then drying at 70 °C to obtain the CSZS−V_{Zn} composite. SiO_2−COOH NPs and Fe_3O_4@Au were synthesized following previously reported studies[26−28] with some improvements (details are provided in the Supporting Information).

Preparation of the Hairpin DNA3 (H3)−SiO_2 NP Complex. For the preparation of H3−SiO_2 NPs, 30 μL of EDC (0.2 M) was added to 15 μL of SiO_2 NPs (2 mg/mL) under stirring for 30 min at 4 °C to activate the carboxylic groups of the SiO_2 NPs. After that, 60 μL of H3 (2.5 μM) labeled with amino groups and 30 μL of NHS (0.05 M) was added to the above solution under stirring overnight to obtain H3−SiO_2 NP complex by cross-linking the activated group of SiO_2 NPs and the amino group of H3.

Target-Induced Enzyme-Assisted Signal Amplification Strategy. First, 100 μL of hairpin DNA1 (H1) and 100 μL of Fe_3O_4@Au were mixed in a tube and then stirred at 4 °C for 12 h to obtain the Fe_3O_4@Au−H1 complex *via* the covalent bond formation of Au−N bonds. Next, the interfering substances of the finished reaction solution were removed by magnetic separation, and then, the obtained Fe_3O_4@Au−H1 complex was scattered in 100 μL of phosphate buffer solution (PBS, pH = 7.0, 0.1 M) for further use. Simultaneously, HT (15 μL, 1 mM) was incubated for blocking the nonspecific adsorption sites. After that, 50 μL of different concentrations of the target was added to the mixed solution and incubated at 37

https://doi.org/10.1021/acs.analchem.1c04820
Anal. Chem. 2021, 93, 17134−17140

°C for 30 min to form the Fe_3O_4@Au−H1−HT−target compound. Subsequently, 3 μL of Exo III (20 U/μL) and 17 μL of 10× NEBuffer 1 were added to the above solution, followed by incubating at 37 °C for 1 h. Eventually, to deactivate the Exo III, the aforementioned solution was heated to 80 °C for 20 min, and the final solution was composed of large amounts of single-strand DNA (output DNA), which was stored at 4 °C for further use.

Fabrication of the PEC Biosensor. The fabrication process is displayed in Scheme 1. Antecedent to modification, the surface of GCE was polished with alumina powder (0.3, 0.05 μm) and then ultrasonically cleaned in ultrapure water and ethanol alternately.[29] Next, the pretreated mirror-like GCE was first coated with 10 μL of photoactive material CSZS−V_{Zn}, followed by drying at 37 °C for obtaining a lightly yellow film. After that, 10 μL of the as-prepared Au NPs was dripped on the electrode surface and desiccated at 37 °C to obtain a Au layer. Subsequently, 15 μL of H2 (3 μM) was anchored on the GCE/CSZS−V_{Zn}/Au layer electrode overnight at 4 °C utilizing the formation of Au−S bonds. After blocking the binding sites with 10 μL of 1 mM HT for 40 min at room temperature, 15 μL of output DNA was added to the modified electrode to form a H2/output DNA hybrid (37 °C for 2 h). Finally, 15 μL of H3 labeled with SiO_2 was introduced into the electrode by the SDR (37 °C and 2 h) to obtain a H2/H3−SiO_2 complex. Completing each modification, the electrode was strictly rinsed with ultrapure water to remove nonspecifically bonded species.

RESULTS AND DISCUSSION

Characterization of Prepared Nanomaterials. The morphologies and sizes of the prepared nanomaterials were analyzed by transmission electron microscopy (TEM) and scanning electron microscopy (SEM). As illustrated in Figure 1A, ZnS−V_{Zn} has an irregular nanoparticle morphology with a small diameter of 50 nm. Figure 1B shows that the surface of ZnS−V_{Zn} became rough, owing to the successful preparation of CSZS−V_{Zn}. Simultaneously, the SEM image of lots of irregular nanoparticles on the surface of ZnS−V_{Zn} (Figure 1C) and the SEM mapping images (Figure S3) confirmed the successful synthesis of CSZS−V_{Zn}.[30] As shown in Figure 1D, SiO_2−COOH NPs with an average size of 40 nm had a spherical structure and showed well-dispersed NPs.[26] These results indicate the successful synthesis of nanomaterials.

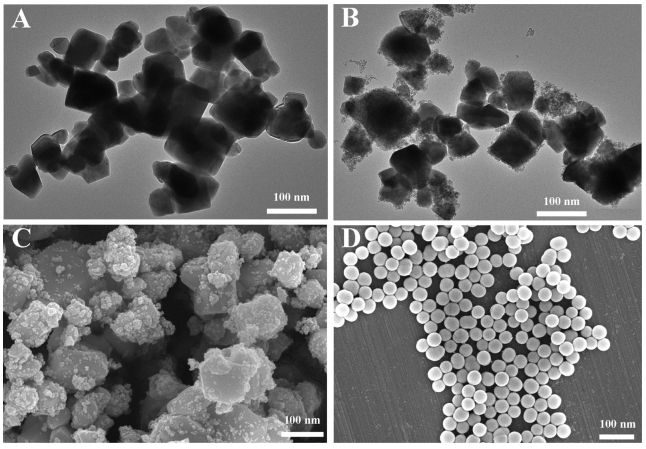

Figure 1. TEM images of ZnS−V_{Zn} (A) and CSZS−V_{Zn} (B) and SEM images of CSZS−V_{Zn} (C) and SiO_2 NPs (D).

Additionally, X-ray diffraction (XRD) analysis of ZnS−V_{Zn}, CdS, and CSZS−V_{Zn} was performed to investigate their chemical compositions and crystallographic structures. As illustrated in Figure 2A, the four major diffraction peaks at 28.59, 33.02, 47.50, and 56.57° in the ZnS−V_{Zn} sample correspond to the cubic zinc blende structure of (111), (200), (222), and (311) crystal planes (JCPDS # 05-0566).[31] Moreover, the diffraction peak positions and intensities of the prepared CdS are consistent with the granular structure (JCPDS # 41-1049).[32] Exhilaratingly, all the diffraction peaks of CdS and ZnS−V_{Zn} phases are reflected in the CSZS−V_{Zn} sample, indicating the successful preparation of the CSZS−V_{Zn} composite.[30] Besides, the constitution and surface chemical states of CSZS−V_{Zn}, ZnS, and CdS nanostructures were investigated *via* X-ray photoelectron spectroscopy (XPS). Compared to the full spectrum of ZnS−V_{Zn} and CdS, the prepared CSZS−V_{Zn} displayed the co-existence of S, C, O, and Zn elements at the corresponding position on the surface (Figure 2B). The Cd 3d, S 2p, and Zn 2p spectra of CSZS−V_{Zn} were comparatively analyzed to further demonstrate the successful synthesis of CSZS−V_{Zn} (Figure S6).

CV and EIS Characterizations of the Developed Biosensor. To demonstrate the stepwise construction processes of the PEC biosensor, cyclic voltammetry (CV) and electrochemical impedance spectroscopy (EIS) were investigated in 5 mM $[Fe(CN)_6]^{3-/4-}$ solution mixed with 0.1 M KCl. As depicted in Figure 3A, the bare GCE presented a pair of well-defined redox peaks (curve a). After CSZS−V_{Zn} was assembled on the GCE, the peak current dramatically decreased (curve b), which occurred mainly because of the charge transfer obstruction of the composite. After Au NPs were immobilized on the electrode surface, the amount of redox currents increased (curve c) because the Au NPs could promote electron transfer. However, the peak currents were slightly decreased with the introduction of negatively charged H2 (curve d) and output DNA (curve f) on the above-mentioned electrode, which could be ascribed to the electronic repulsion between $[Fe(CN)_6]^{3-/4-}$ and DNA sequences. After that, HT was incubated on the electrode, resulting in a further decreased peak current (curve e), primarily caused by the steric hindrance of HT. Finally, the amount of redox peak currents broadly decreased (curve g) with the SiO_2-labeled probes modified on the electrode due to the poor conductivity of SiO_2. The corresponding EIS curves are shown in Figure 3B; a significant increase in the charge-transfer resistance (R_{et}) response (curve b) was monitored, owing to the low-conduction property of CSZS−V_{Zn} compared with the bare GCE (curve a). With the Au NPs being assembled on the GCE/CSZS−V_{Zn} electrode surface, a minimal R_{et} value (curve c) was obtained, mainly because Au NPs had excellent conductivity. After H2, HT, and output DNA were introduced on the electrode surface stepwise, unceasingly increased R_{et} curves (d to f) were recorded due to the poor conductivity of HT and the electrostatic repulsion of nucleotide sequences. Finally, when H3 marked with SiO_2 was modified on the electrode, a sharply enhanced R_{et} (curve g) was observed, which could be attributed to the poor conductivity of SiO_2. These EIS results are corresponding to the CV results, further manifesting the successful fabrication of this sensing platform.

Characterization of PEC Response and PAGE Analysis. PEC response and native polyacrylamide gel electro-

https://doi.org/10.1021/acs.analchem.1c04820
Anal. Chem. 2021, 93, 17134−17140

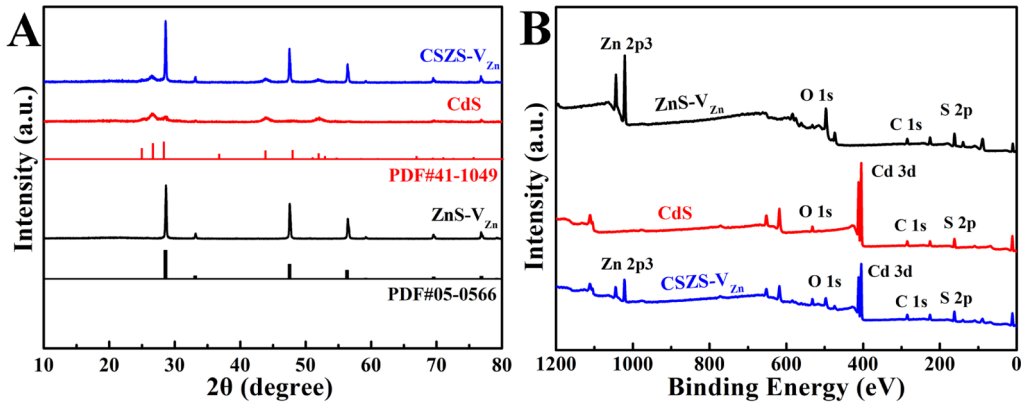

Figure 2. XRD patterns (A) and XPS survey spectra (B) of CdS, ZnS−V_{Zn}, and CSZS−V_{Zn}.

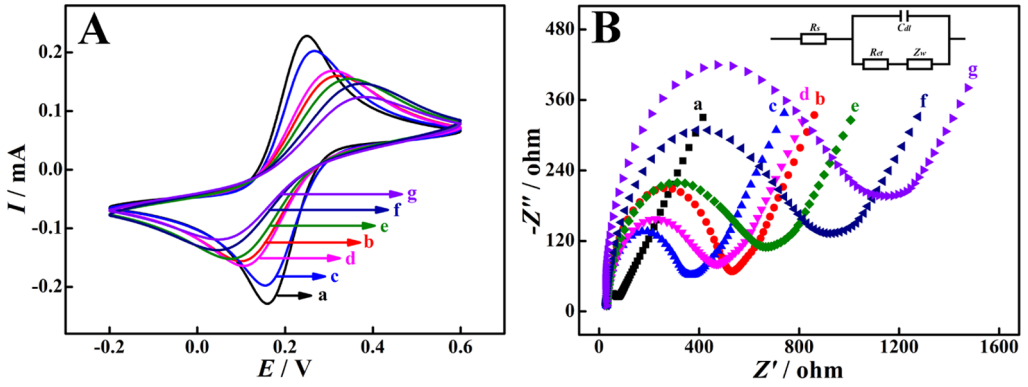

Figure 3. CV (A) and EIS (B) responses of (a) bare GCE, (b) GCE/CSZS−V_{Zn}, (c) GCE/CSZS−V_{Zn}/Au layer, (d) GCE/CSZS−V_{Zn}/Au layer/H2, (e) GCE/CSZS−V_{Zn}/Au layer/H2/HT, (f) GCE/CSZS−V_{Zn}/Au layer/H2/HT/output DNA, and (g) GCE/CSZS−V_{Zn}/Au layer/H2/HT/output DNA/H3−SiO_2.

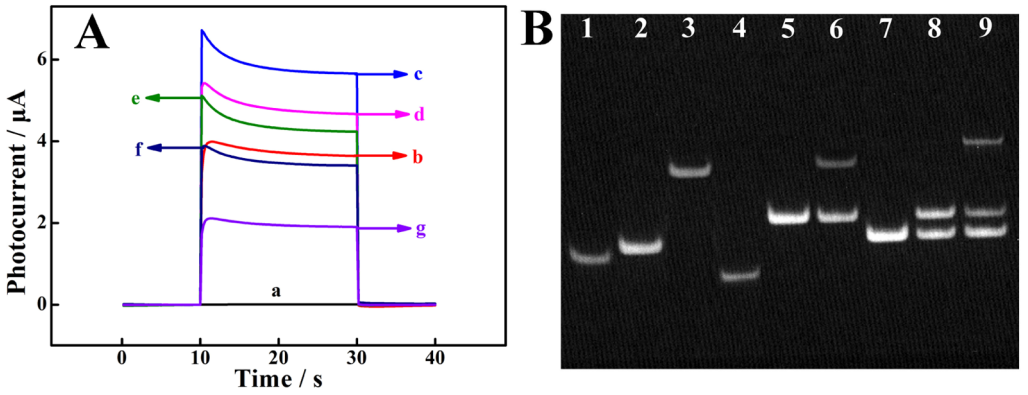

Figure 4. (A) PEC characterization of (a) bare GCE, (b) GCE/CSZS−V_{Zn}, (c) GCE/CSZS−V_{Zn}/Au layer, (d) GCE/CSZS−V_{Zn}/Au layer/H2, (e) GCE/CSZS−V_{Zn}/Au layer/H2/HT, (f) GCE/CSZS−V_{Zn}/Au layer/H2/HT/output DNA, and (g) GCE/CSZS−V_{Zn}/Au layer/H2/HT/output DNA/H3−SiO_2. (B) 16% native PAGE analysis of nucleic samples: lane 1, miRNA-122; lane 2, H1; lane 3, miRNA-122 + H1; lane 4: miRNA-122 + H1 + Exo III; lane 5, H2; lane 6, miRNA-122 + H1 + Exo III + H2; lane 7, H3; lane 8, H2 + H3; and lane 9, miRNA-122 + H1 + Exo III + H2 + H3.

phoresis (PAGE) analysis were executed to further evaluate the successful construction of this biosensor. As depicted in Figure 4A, after coating photoactive material CSZS−V_{Zn} on the bare electrode, a dramatically enhanced photocurrent (curve b) was gained compared with the bare GCE (curve a), which could be ascribed to its eminent conductivity enhancing the separation and photoelectron migration efficiencies. When Au NPs were assembled on the aforementioned electrode, an obviously enhanced PEC response (curve c) was monitored due to the excellent conductivity. With the H2, HT, and output DNA being stepwise dropped on the modified electrode, continuously diminishing photocurrents (curve d to f) were obtained due to the poor charge transfer ability caused by steric hindrance. Eventually, as the SiO_2-labeled H3 was introduced on the modified electrode surface, a distinct decreasing photocurrent signal (curve g) was observed due to the poor conductivity of SiO_2. The aforementioned results further demonstrate the successful fabrication of the developed biosensor. The melting curve (Figure S9) of the target coupling showed that the melting temperature was around 45

https://doi.org/10.1021/acs.analchem.1c04820
Anal. Chem. 2021, 93, 17134−17140

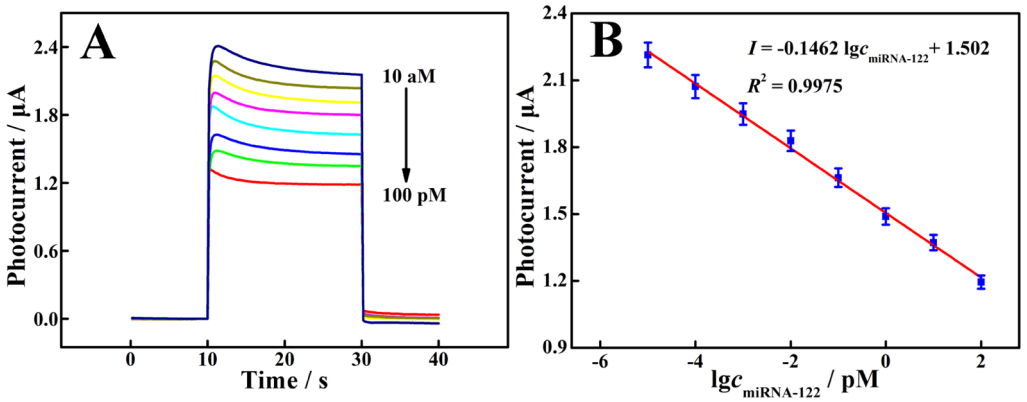

Figure 5. (A) Photocurrent response of the biosensor with different miRNA-122 concentrations: 10 aM, 100 aM, 1 fM, 10 fM, 100 fM, 1 pM, 10 pM, and 100 pM. (B) Corresponding linear calibration curve for miRNA-122 detection at various concentrations.

°C. Moreover, PAGE analysis was conducted to demonstrate the feasibility of the designed Exo III-assisted signal amplification process and SDR. As shown in Figure 4B, the target (miRNA-122) and H1 in lanes 1 and 2 represent a distinct single band, respectively. When miRNA-122 was mixed with H1, a new bright band with a slower movement in lane 3 compared to lanes 1 and 2 appeared, which could be attributed to the hybridization product of miRNA-122 and H1. With the presence of Exo III, a new band which exhibited a faster movement and a low molecular weight (lane 4) appeared, indicating the successful generation of output DNA with assistance from Exo III. Additionally, lane 5 and lane 7 represented two single-chain bands of H2 and H3. Compared with lane 4 and lane 5, lane 6 showed a new band with a slower moving speed, confirming the successful hybridization of output DNA and H2. Lane 8 showed the PAGE result in the presence of equivalent amounts of HP2 and HP3, suggesting that HP2 and HP3 could not pair without target miRNA-122. Comparatively speaking, a new band with a slower move rate and higher molecular weight appeared (lane 9), representing the hybrid product of H2 and H3 in the presence of the target miRNA-122. These results further indicate that the construction of the proposed biosensor and the enzyme-assisted cycle amplification strategy are successful.

Analytical Performance of the Developed Biosensor. Photocurrent responses with different concentrations of miRNA-122 were monitored to evaluate under the optimal conditions of the developed biosensor (Figure S1). As shown in Figure 5A, with an increase in the target miRNA-122 concentration from 10 aM to 100 pM, the photocurrent responses continuously diminished. In addition, the photocurrent responses and the logarithm of target miRNA-122 concentrations showed an excellent linear relationship (Figure 5B), and the corresponding linear regression equation is expressed as $I = -0.1462 \lg c_{miRNA-122} + 1.502$ with a correlation coefficient of 0.9975 (I is the photocurrent intensity and c is the concentration of miRNA-122). On the basis of previous reports, the limit of detection (LOD) was calculated as 3.3 aM. Furthermore, a comparison between this study and some previously reported methods for detecting miRNA-122 is shown in Table 1, suggesting that the constructed PEC biosensor in this study has superior sensitivity.

Selectivity and Stability Studies of the Developed Biosensor. The selectivity and stability of the fabricated biosensor were validated to further prove the performance of this biosensor comprehensively. To evaluate the specificity of the developed biosensor, we contrasted the PEC signal responses of the biosensor unto miRNA-122 with other interfering substances under the same experimental conditions, miRNA-141, miRNA-21, miRNA-182-5p, and miRNA-155. As shown in Figure 6A, the concentration of each interfering substance was 100 times (10 pM) that of miRNA-122 (100 fM). Compared to the blank (background signal without miRNA-122), the PEC signal responses of each interfering substance showed slight changes. Obvious changes in the photocurrent response were observed only in the presence of target miRNA-122, which could be mainly ascribed to the entropy-driven DNA amplifier tenet and the Watson−Crick base pairing principle. In addition, photocurrent response for the base-mismatched miRNA-122 was similar with that for the blank sample (Figure S8). The abovementioned results demonstrate that this biosensor had a high selectivity and specificity for miRNA-122. The stability, which is essential to its practical application especially in a complex biomedical environment, is another crucial parameter to evaluate the reliability of a biosensor. As shown in Figure 6B, considerably stable photocurrent intensity was observed under consecutive periodic "off−on−off" light for 12 cycles with a relative standard deviation (RSD) of 1.2%, indicating the excellent stability of this proposed biosensor.

Table 1. Comparison of Other Methods and This Study for miRNA Detection

analytical method	detection range	LOD	references
fluorescent	10 fM to 1 nM	5 fM	33
fluorescent	1 fM to 100 pM	0.3 fM	34
SERS	1 fM to 100 nM	349 aM	35
ET	20 fM to 1 nM	10 fM	36
EC	0.1 fM to 0.1 μM	53 aM	37
ECL	100 aM to 1 pM	82 aM	38
PEC	100 aM to 1 pM	0.5 fM	39
PEC	10 aM to 100 pM	3.3 aM	present study

Analysis of miRNA-122 in Human Serum. The reliability of the fabricated biosensor for miRNA-122 detection was assessed by monitoring the 50-fold diluted healthy serum samples with various concentrations of target miRNA-122. The results are shown in Table S2. The recovery ranged from 96.8 to 101% and the RSD ranged between 2.5 and 3.5%, indicating that the proposed biosensor has potential application in complex real samples.

https://doi.org/10.1021/acs.analchem.1c04820
Anal. Chem. 2021, 93, 17134−17140

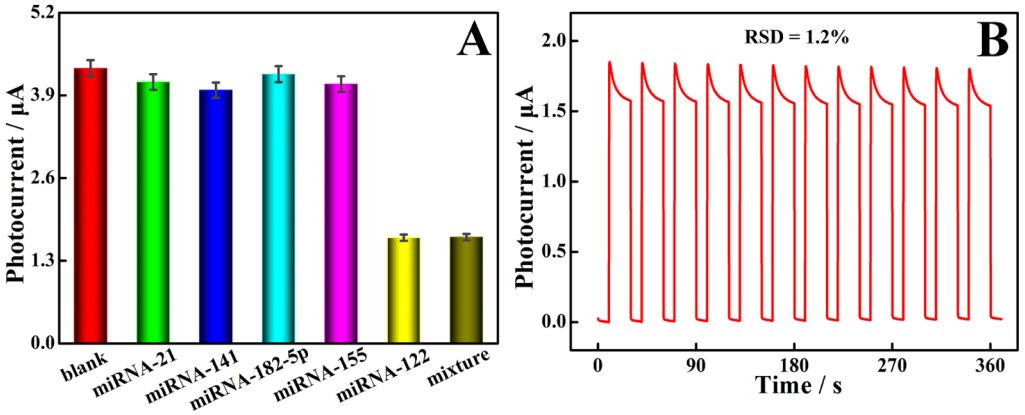

Figure 6. (A) Selectivity of the proposed biosensor to the blank control group and different substances: miRNA-21, miRNA-141, miRNA-182-5p, miRNA-155, the mixture, and target. (B) Stability of the PEC biosensor in the presence of 100 fM miRNA-122 under consecutive periodic "off−on−off" light for 12 cycles.

CONCLUSIONS

In this work, we designed a novel PEC biosensor for miRNA-122 detection based on the signal-off strategy with Z-scheme heterojunctions of Zn-defective-mediated CSZS−V_{Zn} as the photoactive material and SiO_2 as the signal quencher. The CSZS−V_{Zn} heterostructures showed an excellent PEC signal response under visible light, about 8fold and 5fold higher than that of ZnS−V_{Zn} and CdS, respectively, indicating efficient separation and charge carrier migration. Significantly, the elaborated PEC biosensor demonstrated a high sensitivity and low detection limit by utilizing the Exo III-assisted signal amplification strategy and SDR. The developed biosensor not only provides a new method for miRNA-122 assay but also provides a universal pathway for bioanalysis and clinical diagnosis.

ASSOCIATED CONTENT

Supporting Information

The Supporting Information is available free of charge at https://pubs.acs.org/doi/10.1021/acs.analchem.1c04820.

Materials and reagents, sequences used in the experiment, apparatus, PEC measurement, native PAGE analysis process, RNA coupling melting analysis, synthesis of SiO_2−COOH NPs and Fe_3O_4@Au, optimization of the experimental conditions, comparison of PEC responses for different photoactive materials, characterization of CdS and CSZS−V_{Zn}, mechanism of charge transfer, optical characterizations of the nanomaterial, XPS analysis of specific elements of nanomaterials, PL characterizations of the nanomaterial, specificity test of the developed biosensor, melting analysis of target coupling, and analysis of miRNA-122 in human serum (PDF).

AUTHOR INFORMATION

Corresponding Author

Fengli Qu − *Department of Pathology, Cancer Hospital of the University of Chinese Academy of Sciences, Institute of Basic Medicine and Cancer, Chinese Academy of Sciences, Hangzhou 310022 Zhejiang, China; College of Chemistry and Chemical Engineering, Qufu Normal University, Qufu 273165 Shandong, China;* orcid.org/0000-0001-6311-3051; Phone: +86 537 4456301; Email: fengliquhn@hotmail.com; Fax: (+86) 537 4456301

Authors

Xiankang Niu − *Department of Pathology, Cancer Hospital of the University of Chinese Academy of Sciences, Institute of Basic Medicine and Cancer, Chinese Academy of Sciences, Hangzhou 310022 Zhejiang, China; College of Chemistry and Chemical Engineering, Qufu Normal University, Qufu 273165 Shandong, China*

Yan Zhao − *College of Chemistry and Chemical Engineering, Qufu Normal University, Qufu 273165 Shandong, China*

Fang Wang − *College of Chemistry and Chemical Engineering, Qufu Normal University, Qufu 273165 Shandong, China*

Jinghua Wu − *College of Chemistry and Chemical Engineering, Qufu Normal University, Qufu 273165 Shandong, China*

Weihong Tan − *Department of Pathology, Cancer Hospital of the University of Chinese Academy of Sciences, Institute of Basic Medicine and Cancer, Chinese Academy of Sciences, Hangzhou 310022 Zhejiang, China;* orcid.org/0000-0002-8066-1524

Complete contact information is available at: https://pubs.acs.org/10.1021/acs.analchem.1c04820

Notes

The authors declare no competing financial interest.

ACKNOWLEDGMENTS

This work was financially supported by the National Natural Science Foundation of China (21775089 and 22074080), the Changjiang Scholar Program of the Ministry of Education of China (Q2019258), and the Taishan Scholar Program of Shandong Province (tsqn201909106).

REFERENCES

(1) Victorious, A.; Saha, S.; Pandey, R.; Soleymani, L. *Angew. Chem., Int. Ed. Engl.* **2021**, *60*, 7316−7322.
(2) Li, H.; Han, M.; Weng, X.; Zhang, Y.; Li, J. *ACS Nano* **2021**, *15*, 1710−1717.
(3) Zhao, C.-Q.; Zhou, J.; Wu, K.-W.; Ding, S.-N.; Xu, J.-J.; Chen, H.-Y. *Anal. Chem.* **2020**, *92*, 6886−6892.
(4) Victorious, A.; Saha, S.; Pandey, R.; Didar, T. F.; Soleymani, L. *Front. Chem.* **2019**, *7*, 617.
(5) Qiu, Z.; Shu, J.; Tang, D. *Anal. Chem.* **2018**, *90*, 12214−12220.

(6) Sun, Y.; Zhang, Y.; Zhang, H.; Liu, M.; Liu, Y. *Anal. Chem.* **2020**, *92*, 10668−10676.
(7) Chen, H.; Rim, Y. S.; Wang, I. C.; Li, C.; Zhu, B.; Sun, M.; Goorsky, M. S.; He, X.; Yang, Y. *ACS Nano* **2017**, *11*, 4710−4718.
(8) Tan, J.; Peng, B.; Tang, L.; Zeng, G.; Lu, Y.; Wang, J.; Ouyang, X.; Zhu, X.; Chen, Y.; Feng, H. *Anal. Chem.* **2020**, *92*, 13073−13083.
(9) Hatchett, D. W.; Josowicz, M. *Chem. Rev.* **2008**, *108*, 746−769.
(10) Lupan, O.; Postica, V.; Wolff, N.; Polonskyi, O.; Duppel, V.; Kaidas, V.; Lazari, E.; Ababii, N.; Faupel, F.; Kienle, L.; Adelung, R. *Small* **2017**, *13*, 1602868.
(11) Liu, M.; Jing, D.; Zhou, Z.; Guo, L. *Nat. Commun.* **2013**, *4*, 2278.
(12) Li, H.; Zhou, Y.; Tu, W.; Ye, J.; Zou, Z. *Adv. Funct. Mater.* **2015**, *25*, 998−1013.
(13) Wang, L.; Karuturi, S.; Zan, L. *Small* **2021**, *17*, 2101833.
(14) Varghese, A.; Saha, D.; Thakar, K.; Jindal, V.; Ghosh, S.; Medhekar, N. V.; Ghosh, S.; Lodha, S. *Nano Lett.* **2020**, *20*, 1707−1717.
(15) Wei, L.; Yu, C.; Zhang, Q.; Liu, H.; Wang, Y. *J. Mater. Chem. A.* **2018**, *6*, 22411−22436.
(16) Cho, S.-Y.; Jang, D.; Kang, H.; Koh, H.-J.; Choi, J.; Jung, H.-T. *Anal. Chem.* **2019**, *91*, 6850−6858.
(17) Xu, Q.; Zhang, L.; Cheng, B.; Fan, J.; Yu, J. *Chem.* **2020**, *6*, 1543−1559.
(18) Selim, S.; Pastor, E.; García-Tecedor, M.; Morris, M. R.; Francàs, L.; Sachs, M.; Moss, B.; Corby, S.; Mesa, C. A.; Gimenez, S.; Kafizas, A.; Bakulin, A. A.; Durrant, J. R. *J. Am. Chem. Soc.* **2019**, *141*, 18791−18798.
(19) Lee, Y.-L.; Lo, Y.-S. *Adv. Funct. Mater.* **2009**, *19*, 604−609.
(20) Lee, Y.-L.; Chi, C.-F.; Liau, S.-Y. *Chem. Mater.* **2009**, *22*, 922−927.
(21) Jia, X.; Tahir, M.; Pan, L.; Huang, Z.-F.; Zhang, X.; Wang, L.; Zou, J.-J. *Appl. Catal., B* **2016**, *198*, 154−161.
(22) Wang, S.; Pan, L.; Song, J.-J.; Mi, W.; Zou, J.-J.; Wang, L.; Zhang, X. *J. Am. Chem. Soc.* **2015**, *137*, 2975−2983.
(23) Hao, X.; Wang, Y.; Zhou, J.; Cui, Z.; Wang, Y.; Zou, Z. *Appl. Catal., B* **2018**, *221*, 302−311.
(24) Çetin, B.; Song, G. J.; O'Leary, S. E. *J. Am. Chem. Soc.* **2020**, *142*, 21249−21253.
(25) Law, A. S.-Y.; Lee, L. C.-C.; Lo, K. K.-W.; Yam, V. W.-W. *J. Am. Chem. Soc.* **2021**, *143*, 5396−5405.
(26) Wang, H.; Li, M.; Zheng, Y.; Hu, T.; Chai, Y.; Yuan, R. *Biosens. Bioelectron.* **2018**, *120*, 71−76.
(27) Niu, X.; Lu, C.; Su, D.; Wang, F.; Tan, W.; Qu, F. *Anal. Chem.* **2021**, *93*, 13727−13733.
(28) Xie, S.; Dong, Y.; Yuan, Y.; Chai, Y.; Yuan, R. *Anal. Chem.* **2016**, *88*, 5218−5224.
(29) Xia, L.-Y.; Li, M.-J.; Wang, H.-J.; Yuan, R.; Chai, Y.-Q. *Anal. Chem.* **2020**, *92*, 14550−14557.
(30) Yu, K.; Huang, H.-B.; Wang, J.-T.; Liu, G.-F.; Zhong, Z.; Li, Y.-F.; Cao, H.-L.; Lü, J.; Cao, R. *J. Mater. Chem. A.* **2021**, *9*, 7759−7766.
(31) Zhou, Q.; Li, L.; Xin, Z.; Yu, Y.; Wang, L.; Zhang, W. *J. Alloys Compd.* **2020**, *813*, 152190.
(32) Liu, F.; Xiao, C.-X.; Meng, L.-H.; Chen, L.; Zhang, Q.; Liu, J.-B.; Shen, S.; Guo, J.-K.; Au, C.-T.; Yin, S.-F. *ACS Sustainable Chem. Eng.* **2020**, *8*, 1302−1310.
(33) Zhang, H.; Huang, X.; Liu, J.; Liu, B. *Chem. Sci.* **2020**, *11*, 3812−3819.
(34) Qi, T.; Song, C.; He, J.; Shen, W.; Kong, D.; Shi, H.; Tan, L.; Pan, R.; Tang, S.; Lee, H. K. *Anal. Chem.* **2020**, *92*, 5033−5040.
(35) Wu, J.; Zhou, X.; Li, P.; Lin, X.; Wang, J.; Hu, Z.; Zhang, P.; Chen, D.; Cai, H.; Niessner, R.; Haisch, C.; Sun, P.; Zheng, Y.; Jiang, Z.; Zhou, H. *Anal. Chem.* **2021**, *93*, 8799−8809.
(36) Chen, L.; Zhang, Q.; Liu, W.; Xiao, H.; Liu, X.; Fan, L.; Wang, Y.; Li, H.; Cao, C. *Biosens. Bioelectron.* **2021**, *171*, 112676.
(37) Guo, Q.; Yu, Y.; Zhang, H.; Cai, C.; Shen, Q. *Anal. Chem.* **2020**, *92*, 5302−5310.
(38) Xu, Z.-H.; Gao, H.; Zhang, N.; Zhao, W.; Cheng, Y.-X.; Xu, J.-J.; Chen, H.-Y. *Anal. Chem.* **2021**, *93*, 1686−1692.
(39) Li, J.; Weng, X.; Mo, F.; Han, M.; Li, H. *Anal. Chem.* **2020**, *92*, 15145−15151.

https://doi.org/10.1021/acs.analchem.1c04820
Anal. Chem. 2021, 93, 17134−17140